Nickel metaphosphate $Ni(PO_3)_2$ as a conversion positive electrode for lithium-ion batteries

Dr. Qingbo Xia[1,2], Prof. Dr. Maxim Avdeev[1,2], Assoc. Prof. Dr. Siegbert Schmid[1], Dr. Hongwei Liu[3], Dr. Bernt Johannessen[4], Prof. Dr. Chris D. Ling[1,*]

[1] *School of Chemistry, The University of Sydney, Sydney 2006, Australia*

[2] *Australian Centre for Neutron Scattering, Australian Nuclear Science and Technology Organisation, Lucas Heights 2234, Australia*

[3] *Australian Centre for Microscopy & Microanalysis, The University of Sydney, Sydney 2006, Australia*

[4] *Australian Synchrotron, Australian Nuclear Science and Technology Organisation, Clayton 3168, Australia*

Corresponding Author E-mail: *chris.ling@sydney.edu.au*

Abstract

Lithium storage schemes based on conversion chemistry have been used in a large variety of negative electrodes achieving capacities 2-3 times higher than graphite. However, to date, relatively few positive electrode examples have been reported. Here, we report a new conversion positive electrode, $Ni(PO_3)_2$, and systematic studies on its working and degradation mechanisms. Crystalline $Ni(PO_3)_2$ undergoes an electrochemistry-driven amorphisation process in the first discharge to form a fine microstructure, consisting of Ni domains with ~2 nm wide that form a percolating electron-conducting network, embedded in a glassy $LiPO_3$ matrix. P does not participate electrochemically, remaining as P^{5+} in $[PO_3]^-$ throughout. The electrode does not recrystallise in the following first charge process, remaining amorphous over all subsequent cycles. The low ionicity of the Ni-$[PO_3]$ bond and the high Li^+ conductivity of the $LiPO_3$ glass lead to high intrinsic electrochemical activity, allowing the micro-sized $Ni(PO_3)_2$ to achieve its

theoretical capacity of 247 mAh/g. The performance of the $Ni(PO_3)_2$ electrode ultimately degrades due to the growth of larger and more isolated Ni grains. While the theoretical capacity of $Ni(PO_3)_2$ is itself limited, it sheds new light on the underlying chemical mechanisms of conversion cathodes, an important new class of electrode for solid-state batteries.

Keywords: lithium-ion batteries, $Ni(PO_3)_2$ positive electrode, conversion reaction, electrode degradation, metallic Ni overgrowth

Table of Contents Graphical Abstract (60-80 words)

The working and degradation mechanisms of a new conversion positive electrode, nickel metaphosphate, are systematically studied in this work. $Ni(PO_3)_2$ shows a high intrinsic electrochemical activity due to a well-developed percolating electron-conducting network consisting of fine metallic Ni nanodomains, and a fast Li^+-conducting $LiPO_3$ glass matrix with embedded Ni nanodomains, formed during lithiation. The electrochemical performance of the $Ni(PO_3)_2$ positive electrode ultimately degrades due to the growth of larger and more isolated Ni nanograins.

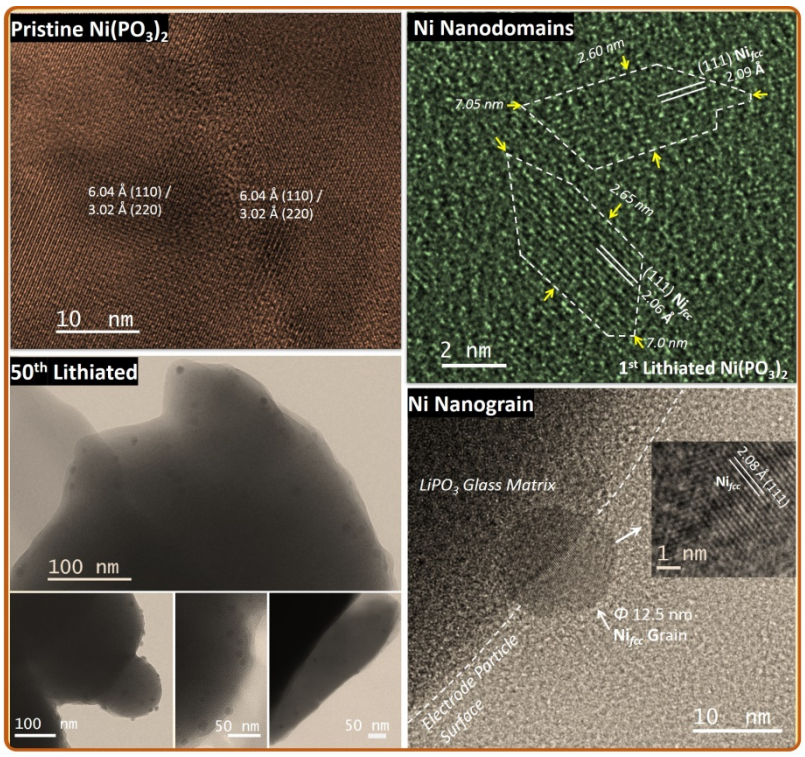

Introduction

Lithium-ion batteries (LIBs) are currently the leading technology for portable electrical energy storage. However, while demand is growing, the pace of fundamental development is arguably slowing [1-2]. A key issue is that the energy densities of commonly used positive electrode materials based on intercalation chemistry - such as layered oxides, spinel oxides, and olivine phosphates - have reached their electrochemical limits [3-4]. Pushing to increase their energy densities entails significant safety issues[5] including runaway oxidation[6] and electrolyte decomposition[7].

Beyond intercalation chemistry, conversion positive electrodes are attractive for their extraordinarily high theoretical capacities [8-14]. Conversion electrodes enable the transfer of ≥2 electrons per electrochemically active atom, versus typically ≤1 in intercalation electrodes.

Significant advances have recently been made. Among them, the sulfur positive electrode is the most studied [12-13]. Sulfur has a huge theoretical capacity of 1675 mAh/g and is accessibly abundant in nature. However, challenges remain for sulfur electrodes, notably low electronic and ionic conductivities, massive volume changes on cycling and the shuttle effect of polysulfides[15]. Sulfur is also flammable, giving rise to safety concerns.

Another conversion positive electrode that has been intensively investigated is iron trifluoride [8-9, 11, 16]. FeF_3 can theoretically react with three Li^+ ions to deliver a high capacity of 712 mAh/g, and iron is inexpensive and abundant. Several issues, however, hinder its practical application. Firstly, fluoride is a toxic substance with the potential to cause bone disease in high concentrations[17]. Secondly, the high ionicity of the Fe-F bond results in a large band gap, making FeF_3 insulating, which severely limits its electrochemical activity. An unacceptably low capacity of 80 mAh/g was achieved when FeF_3 positive electrode was reported for the first time[18]. Nanostructured FeF_3 and nanocomposites [8, 11, 16, 19] with high-conductivity carbon (*e.g.*, carbon fibre and graphene) prepared using elaborate methods have been shown to improve the electrochemical performance, but the practical capacity of FeF_3 is still far from the theoretical value (less than 60%) [9-10, 16, 19-20]. Thirdly, low reversibility of the conversion reaction in FeF_3/Li batteries gives rise to rapid capacity fading. The formation of large metallic Fe domains and crystalline/pseudo-amorphous LiF clusters are thermodynamically favoured during lithiation, and the high activation energy required to break the high-ionicity Li-F bond results in large mass-transport resistance in the following de-conversion process [16].

One way to address the intrinsically low electronic and ionic conductivities of sulfur and FeF_3 as positive electrodes is nanosizing of the particles [10, 12-13, 21]. However, this introduces other problems such as higher synthesis costs, lower volumetric energy densities, and severe

electrolyte decomposition caused by the large specific surface area of nanoparticles[5, 22-23]. The history of lithium-ion batteries shows that materials with low intrinsic electrochemical activities are generally inferior as commercial electrodes. *E.g.*, olivine $LiMnPO_4$ has a higher theoretical energy density but lower electrochemical activity than its homologue $LiFePO_4$, but only the latter has been successfully commercialised [24-25]. Efforts are still required to search for new electrodes with high electrochemical activities and bring conversion electrodes into the real world.

Herein, we report a new conversion positive electrode nickel metaphosphate. The polyanion-type $Ni(PO_3)_2$ electrode has a theoretical capacity of 247 mAh/g on full reduction of Ni^{2+} to metallic Ni^0. While this is lower than that of the monoanion-type fluoride electrode (*e.g.*, 712 mAh/g of FeF_3, and 554 mAh/g of NiF_2 [14]), $Ni(PO_3)_2$ shows much better intrinsic electrochemical activity, due to the much lower ionicity of the bond between the metal and $[PO_3]^-$ (thermochemical radius[26], 2.04 Å) compared to between the metal and F^- (1.33 Å). A high capacity, close to the theoretical value, can be achieved at room-temperature from micro-sized $Ni(PO_3)_2$ powders synthesised by a conventional solid-state method.

Experimental

Synthesis: $Ni(PO_3)_2$ powders were synthesised by a solid-state reaction method in which stoichiometric nickel acetate tetrahydrate ($Ni(CH_3COO)_2.4H_2O$) (BDH, 99%) and ammonium dihydrogen phosphate (AJAX, 98%) are well-mixed by ball milling at 400 rpm for 2h and then sequentially heated at 400°C for 5 h and 700°C for 10 h with an intermediate re-grinding. Before preparing electrodes, the as-made $Ni(PO_3)_2$ powders were ball-milled at 400 rpm for 1 h to break up aggregates.

Structural and Morphological Characterisations: A PANalytical X-Pert Pro diffractometer was used to confirm the crystal structures and phase purities of the samples. X-ray powder diffraction (XRD) data were collected over a 2θ range of 10–70° in reflection mode under Cu Kα (λ = 1.5406 Å) monochromatic radiation. Rietveld-refinement against the XRD data of as-made $Ni(PO_3)_2$ was performed using TOPAS 5. *Ex situ* XRD data were also collected from the first lithiated and first delithiated electrodes. A Zeiss Sigma FEG Scanning Electron Microscope (SEM) was used to collect micrographic images of the $Ni(PO_3)_2$ samples before and after ball-milling.

Electrochemical Characterisations: The $Ni(PO_3)_2$ positive-electrode slurry was prepared by adding polyvinylidene difluoride (PVDF) binder (Aldrich) and conductive carbon super-P (Alfa Aesar) to the as-made $Ni(PO_3)_2$ powder in a solvent of 1-methyl 2-pyrrolidinone (NMP) (Alfa Aesar) in a mass ratio of 1:1:8. The slurry was stirred overnight and then cast onto aluminium foil with a loading density of ~3 mg/cm^2 with respect to $Ni(PO_3)_2$. After drying at 80°C for 10 h, the electrode film was cut into round disks with a diameter of 16 mm.

CR2032 coin cells of the $Ni(PO_3)_2$ electrode versus Li metal ($Ni(PO_3)_2$/Li cells) were assembled in an Ar-filled glovebox using Celgard polypropylene films (MTI) as separators and 1 M lithium hexafluorophosphate ($LiPF_6$) solution (Sigma-Aldrich) in the mixed solvents of ethylene carbonate (EC) and diethyl carbonate (DEC) in a volume ratio of 1:1 as the electrolyte. The cyclicity and rate capability measurements were performed on a Neware battery testing system over the voltage range of 1.0-3.7 V at room temperature. Cyclic voltammetry (CV) and electrochemical impedance spectroscopy (EIS) measurements were performed using a BioLogic SP300 Potentiostat. We defined the current rate of 1C as 250 mA/g.

Synchrotron X-ray Studies: *In situ* X-ray absorption near-edge spectroscopy (XANES) measurements were carried out on the XAS beamline at Australian Synchrotron to track changes in the valence state of Ni during the first discharge and charge processes. Ni K-edge (E_0 = 8332.8 eV) XANES data were collected in transmission mode under a He atmosphere at room temperature every three hours during the first discharge period and at the ends of both the first discharge and the first charge. The same cell was used for all XANES measurements and the cell was discharged and charged at a current rate of 0.1 C on a Neware battery tester at the beamline. XANES data were processed using the Demeter software suite. *Ex situ* XANES data were collected from delithiated electrodes at the 10^{th}, 20^{th}, 30^{th}, 40^{th}, and 50^{th} cycles, which were prepared in-house in advance of XANES measurements and sealed by Kapton tapes in an Ar-filled glovebox to avoid oxidization during the sample transfer and measurement. To make the comparisons as valid as possible, these electrodes were selected to have exactly the same mass of 6.4 g when fresh.

In situ X-ray powder diffraction (XRPD) measurements were performed on the Powder Diffraction (PD) beamline at the Australian Synchrotron to monitor the phase transformation of $Ni(PO_3)_2$ during the first discharge. Data were collected using monochromatic high-energy X-rays of 18 keV (λ = 0.6888 Å). The cell used for *in situ* XRD measurements was discharged at a current rate of 0.1 C.

Modified CR2032 coin cells were used for *in/ex situ* synchrotron measurements with 4 mm-diameter windows cut on both-side cases and spacers to allow X-ray transfer through the $Ni(PO_3)_2$ electrodes. The windows on cases are sealed using Kapton tapes. The electrode composition and coin-cell structure were the same as for the cells used for electrochemical measurements.

X-ray Photoelectron Spectroscopy (XPS) and Fourier-Transform Infrared (FTIR) Spectroscopy: XPS spectra were collected on a Thermo Fisher Scientific K-Alpha system for the $Ni(PO_3)_2$ powder sample, the pristine and the 1st dis/charged electrode samples, using an X-ray beam diameter of 400 μm. FTIR spectra for these samples were collected on a Shimadzu IRSpirit Fourier-transform infrared spectrophotometer. The 1st dis/charged electrodes were washed using dimethyl carbonate (DMC) three times to remove electrolyte precipitates and/or decomposition products before XPS and FTIR measurements.

High-Resolution Transmission Electron Microscopy (HRTEM): Micrographic images of $Ni(PO_3)_2$ particles were taken on a JEOL JEM-2200FS TEM equipped with an energy-dispersive X-ray spectrometer (EDS) (Bruker Nano GmbH Berlin, Germany) in pristine form, following the 1st lithiation, the 1st delithiation, and the 50th lithiation, respectively. Selected-area electron diffraction (SAED) patterns were also collected from particles following the 1st lithiation, and elemental mapping images were recorded from particles following the 1st delithiation.

Results and Discussion

$Ni(PO_3)_2$ crystallises in the monoclinic space group $C2/c$ [27]. Its framework is comprised of Ni-O chains (constructed by edge-shared $[NiO_6]$ octahedra) and $[P_4O_{12}]$ rings (constructed by four corner-shared $[PO_4]$ tetrahedra), as shown in Figure 1a. The as-made bulk powders of $Ni(PO_3)_2$ demonstrate high phase purity, as evidenced by the excellent Rietveld fit (R_{wp} = 3.94%) to XRD data. As shown in Figure 1b-d, as-made $Ni(PO_3)_2$ has primary particle sizes of 0.5-2 μm while secondary particle sizes are in the order of tens of micrometres. After ball-milling, the large aggregate has been broken up and the primary particles become smaller (≤ 1 μm).

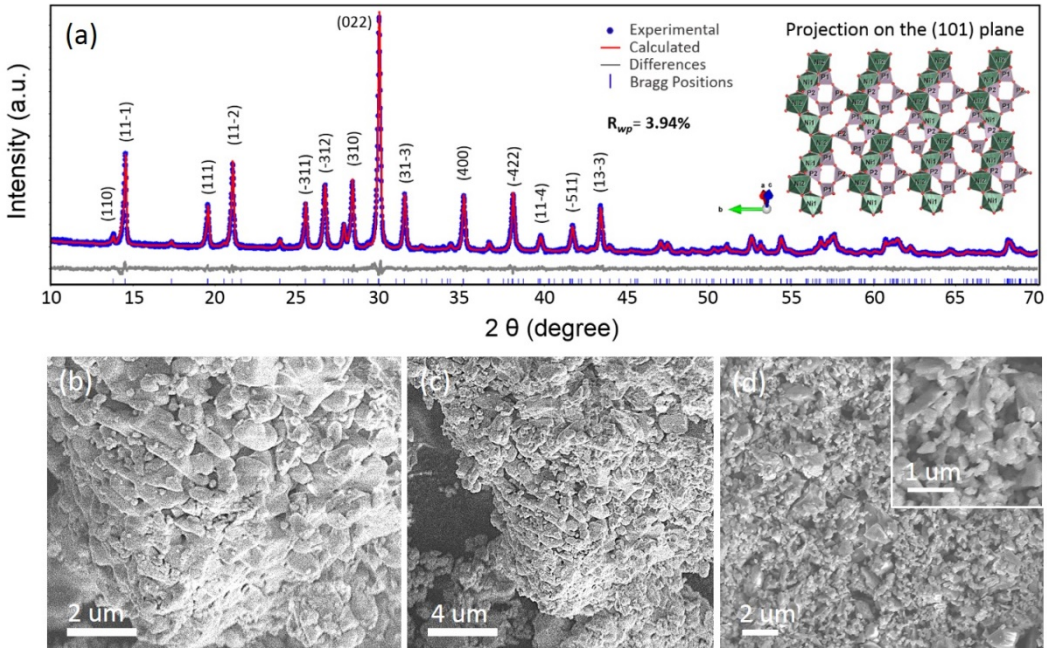

Figure 1 (a) Rietveld-refinement against XRD data (λ = 1.5406 Å) for as-made $Ni(PO_3)_2$, and the refined crystal structure of $Ni(PO_3)_2$ projected on the (101) plane. The refinement yields an excellent profile fit with R_{wp} = 3.94%. SEM images of $Ni(PO_3)_2$ powders (b-c) before and (d) after ball-milling.

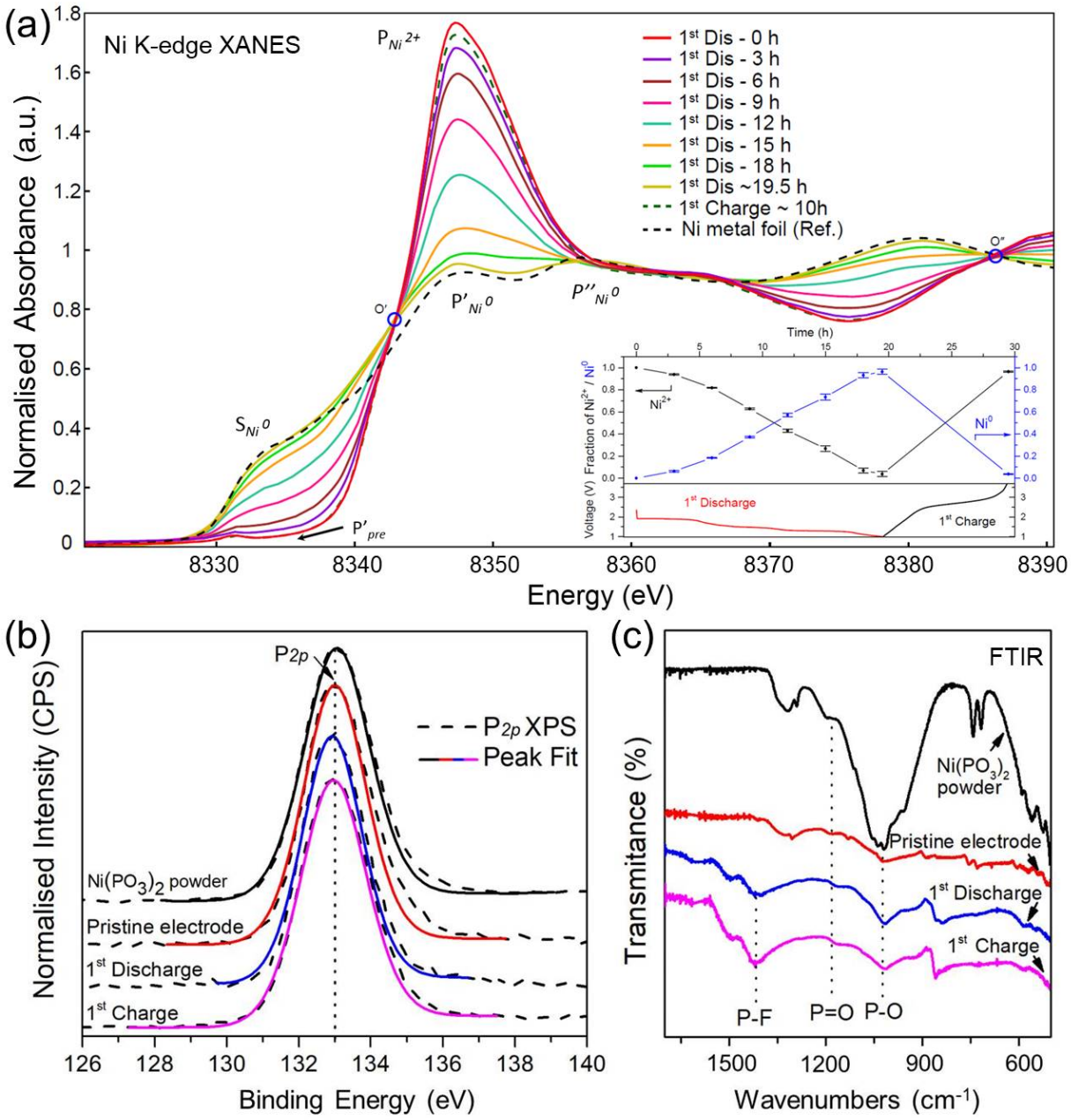

Figure 2 (a) *In situ* XANES spectra (Ni K-edge) collected on the $Ni(PO_3)_2$ electrode every 3h during the first discharge and at the ends of the first discharge and first charge. The inset shows the fractions of Ni^{2+} & Ni^{0} (with error bars) obtained by linear combination fitting to the XANES spectra over the same period. (b) P_{2p} regions of XPS spectra. (c) FTIR spectra of the $Ni(PO_3)_2$ powder, the pristine and the 1st dis/charged electrodes.

In situ XANES measurements were performed on the $Ni(PO_3)_2$/Li conversion cell to gain insight into the Ni redox reaction at the $Ni(PO_3)_2$ positive electrode during the first discharge and charge. As shown in Figure 2, the Ni K-edge spectrum of the pristine $Ni^{2+}(PO_3)_2$ electrode exhibits a strong leading absorption peak (1s absorption) at 8347.6 eV (P_{Ni}^{2+}) in the main-edge region, and a weak peak (1s-3d transition) at 8331.5 eV (P'_{pre}) in the pre-edge region. These are typical features at the Ni K-edge in divalent Ni(II) compounds [28]. Distinct absorption behaviours are noticed compared to the XANES spectrum of our reference Ni^0 metal foil, notably a shoulder at 8335.2 eV (S_{Ni}^0) and two broad peaks at 8347.2 eV (P'_{Ni}^0) and 8356.2 eV (P''_{Ni}^0) respectively in the main-edge region.

On discharging, a progressive evolution is observed in the form of the spectra which change from Ni^{2+}-like to Ni^0-like, indicative of a two-phase reaction from $Ni^{2+}(PO_3)_2$/Li to $LiPO_3$&Ni^0 during the first lithiation. Specifically: the peak of the leading absorption (P_{Ni}^{2+}) gradually shifts to slightly lower energies and finally locks in at ~8347.2 eV (very close to P'_{Ni}^0) at the end of the discharge; while its peak intensity decreases dramatically from 1.76 to 0.94 a.u., and the absorption in the energy range from 8330 eV to 8340 eV gradually increases to form a shoulder (very similar to S_{Ni}^0). The presence of two isosbestic points (O' and O'') formed by all spectra collected from the $Ni(PO_3)_2$ positive electrode further supports the conclusion that a single two-phase transition, *i.e.*, directly from Ni^{2+} to Ni^0 with no Ni^{1+} intermediate, takes place during the conversion reaction.

Linear-combination fittings (LCF) to the spectra were performed using the spectra of the 0 h and the Ni foil as two standards to estimate changes of the fractions of Ni^{2+} and Ni^0 in the $Ni(PO_3)_2$ electrode over the course of the first discharge. As shown in the inset to Figure 2, both Ni^{2+} and Ni^0 fractions change linearly with time, but slower change rates are observed at the beginning and

the end compared to the intermediate period. This indicates that the conversion kinetics of $Ni(PO_3)_2$ with Li are not constant during the reaction, but experience a short acceleration period before a long relatively stable period and then a short deceleration period. The fraction of Ni^0 is 0.963±0.023 at the end of the first discharge, which corresponds to nearly complete lithiation of $Ni(PO_3)_2$. In the following charge cycle, these changes are reversed, whereby the leading edge peak shifts back to 8347.6 eV and the spectrum changes back to almost overlap with that of the pristine $Ni(PO_3)_2$ electrode: the fraction of Ni^{2+} at the end of the first charge at 0.1 C is 0.964±0.004. These results verify a reversible Ni redox reaction ($Ni^{2+} \rightleftharpoons Ni^0$) in the $Ni(PO_3)_2$ electrode over a round-trip dis-/charge cycle.

We performed XPS and FTIR measurements to confirm that the valence state and local bonding environment of P does not change during the electrochemical reaction of $Ni(PO_3)_2$. The XPS spectra in Figure 2b show that the P_{2p} peaks of the pristine, 1st discharged, and 1st charged electrode samples are found at the same binding energy (~133 eV) and have the same shapes. This confirms that the valence state of P does remains +5 during dis/charging. Figure 5c shows FTIR results, in which the stretching vibration peaks of P=O at 1183 cm^{-1} and P-O at 1018 cm^{-1} are observed in the spectra for all these samples, confirming that P stays as $[PO_3]$ during dis/charging. Due to the presence of residual $LiPF_6$ precipitate (from the electrolyte) and/or its decomposition products, the stretching vibration peaks of P-F at 1418 cm^{-1} are also observed in the spectra of dis/charged electrodes. Thus, we can be confident that P remains as P^{5+} in $[PO_3]^-$. (Note that its reduction is unlikely under these electrochemical conditions, and would increase the theoretical capacity of $Ni(PO_3)_2$ to anomalously high values, as presented in Table S2.)

The conversion chemistry in LIBs based on binary transition metal compounds can be generalised in the following equation [4-5]: $M_a^{m+}X_b^{n-} + (b \cdot n)Li^+ + (a \cdot m)e^- \rightleftharpoons aM^0 +$

$b\mathrm{Li}_n^{1+}\mathrm{X}^{n-}$, where M = transition metal, X = anion, and m, n is the valence state of M, X respectively. Based on our XANES, XPS and FTIR data, we suggest that $Ni(PO_3)_2$ reacts with Li^+ following the equation : $\mathrm{Ni(PO_3)_2 + 2\,Li^+ + 2\,e^- \rightleftharpoons Ni^0 + 2\,LiPO_3}$. It is significant to note that the Li salt (Li_nX) formed, $LiPO_3$, is an excellent Li^+ conductor[29]. This should aid the kinetics of the deconversion reaction for $Ni(PO_3)_2$ electrode, and hence the rate performance of the $Ni(PO_3)_2$/Li conversion system.

HRTEM observations were then made to investigate the morphology, short-range ordering, and spatial distribution changes of the phases in the $Ni(PO_3)_2$ positive electrode during the first conversion-deconversion cycle. The HRTEM image of the as-made $Ni(PO_3)_2$ powder in Figure 3a shows long-range ordered lattice fringes which reveal a high degree of crystallinity in the pristine $Ni(PO_3)_2$ electrode. HRTEM investigations on the first lithiated $Ni(PO_3)_2$ electrode demonstrate that metallic Ni nanodomains form during the conversion reaction, embedded in a matrix of amorphous/glassy $LiPO_3$. As depicted in Figure 3b-c, the Ni nanodomains are very small, with sizes varying from sub-nanometre to a few nanometres. The two relatively large-domain regions indicated by polygons in Figure 3c are ~7 nm in length and ~2.6 nm in width, and few much smaller domains can be found around them. These variably sized Ni nanodomains form a percolating Ni network through which electrons can be transported rapidly in the subsequent charge process. In contrast to conversion electrodes where the equivalent metal domains are closely aligned to the crystal lattice of the parent compound [9], the Ni nanodomains here are orientated randomly. This is likely due to a rapid migration of Ni^{2+} out of the $Ni(PO_3)_2$ lattice during the conversion process, so that Ni metal is nucleated randomly. Note that the Ni metal formed in the first discharge process is in a high thermodynamic energy state, indicated by abundant defects in the nanodomains (atoms missing or misplaced in every lattice fringe in

Figure 3c) and irregular boundaries (hinting a high surface energy). Such metastable Ni metal allows the electrode to more easily overcome the de-conversion energy barrier in the following charge process and consequently to achieve a high reversible capacity.

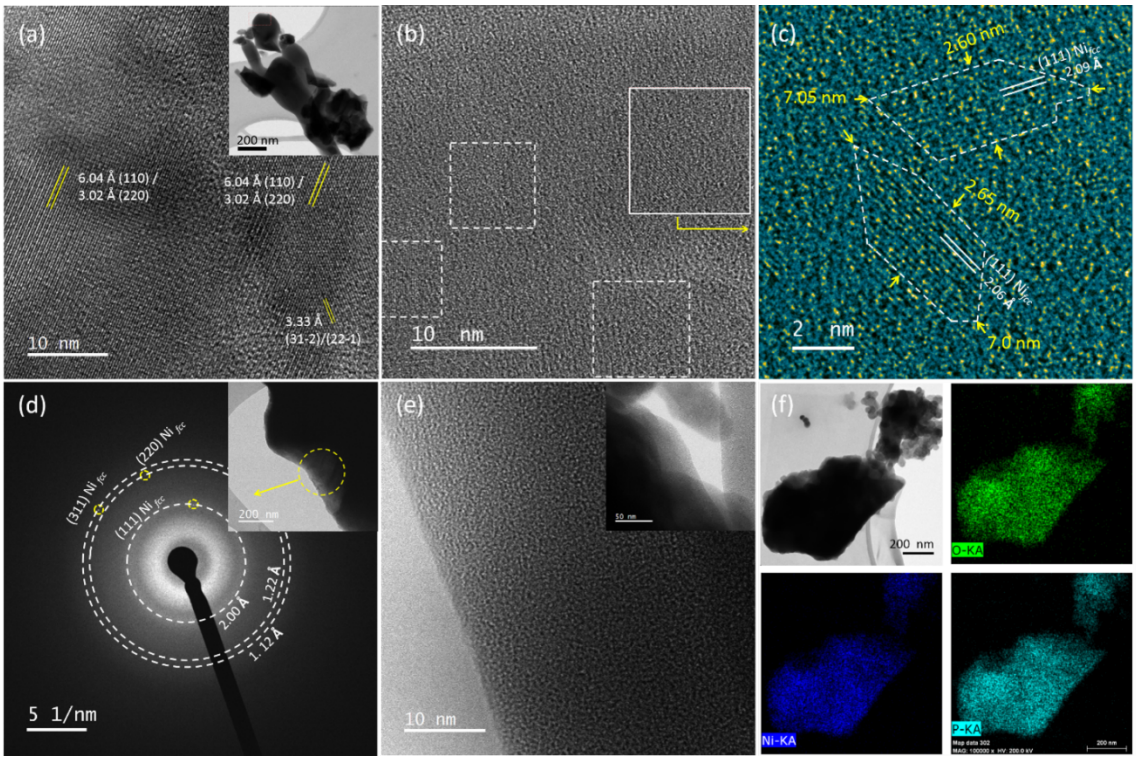

Figure 3 Local structure and phase distribution changes of the $Ni(PO_3)_2$ positive electrode during the first lithiation-delithiation cycle: (a) HRTEM images of pristine $Ni(PO_3)_2$ particles; (b)-(d) HRTEM images and the SAED pattern of a lithiated $Ni(PO_3)_2$ particle after the first discharge (several obvious metallic Ni nanograins are indicated by rectangles in (b), (c) is the magnification of the solid-line rectangle area in (b), and (d) shows the SAED pattern of the yellow circle area on the lithiated $Ni(PO_3)_2$ particle); (e) HRTEM images and (f) Ni, P and O elemental maps of de-lithiated $Ni(PO_3)_2$ particles after the first charge.

The *d*-spacing of the lattice fringes (2.06 Å and 2.09 Å) in two large nanodomains are consistent with $d_{(111)}$ = 2.034 Å for the face-centred cubic (fcc) crystal structure of Ni (ICDD # 64989). This is further confirmed by the selected area electron diffraction (SAED) pattern shown in Figure 3d. Three visible spots in the pattern can be attributed to the (111), (220) and (311) reflections of $Ni_{fcc.}$ No diffraction spots from $Ni(PO_3)_2$ are observed, supporting complete lithiation in the first discharge process. Furthermore, no diffraction spots from $LiPO_3$ are observed, only weak diffuse rings. This suggests that $LiPO_3$ formed in the lithiated electrode is fully amorphous/glassy. $LiPO_3$ glass is a good lithium-ion conductor which has been intensively investigated as a candidate solid-state electrolyte [30-31].

The HRTEM image of the first delithiated $Ni(PO_3)_2$ positive electrode in Figure 3e does not show any evidence for the presence of crystalline phases. This indicates that the Ni metal formed in the first lithiation process has been converted back to $Ni(PO_3)_2$. Note, however, that although no crystal lattice fringes of $Ni(PO_3)_2$ were observed by TEM, we cannot definitely state that the reformed $Ni(PO_3)_2$ is fully amorphous. In our earlier measurements of the pristine material, we found that the loose framework structure of $Ni(PO_3)_2$ is very sensitive to the high-energy electron beam, such that any short-range ordering of the reformed $Ni(PO_3)_2$ would likely be destroyed before it could be observed. The amorphous nature of the de-lithiated electrode is also not completely confirmed by XRD (Figure S1), because while no diffraction peaks of crystalline $Ni(PO_3)_2$ are visible, the size of the domains could be too small to coherently scatter. To rule out any composition changes and elemental segregations in the delithiated $Ni(PO_3)_2$ positive electrode, we performed EDS measurements. The collected spectra in the Supporting Information (Table S1) quantitatively demonstrate that the delithiated electrode has the same

Ni:P ratio of 1 : 2 as $Ni(PO_3)_2$. Elemental maps in Figure 3f clearly show homogeneous distributions of Ni, P and O in the reformed $Ni(PO_3)_2$ particles.

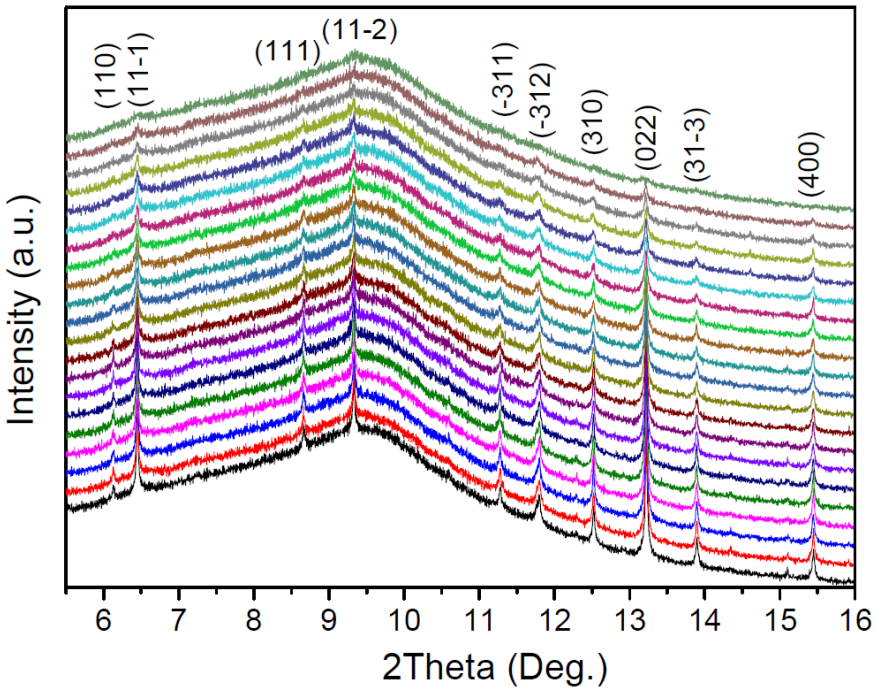

Figure 4 *In situ* synchrotron XRPD patterns (λ = 0.6888 Å) collected on the $Ni(PO_3)_2$ electrode over the first discharge. For clarity, only every 10th data set collected is shown. Patterns are stacked chronologically from the bottom to the top in the figure.

In situ synchrotron XRPD measurements were then performed on a $Ni(PO_3)_2$/Li cell to track phase changes during the first discharge. Figure 4 shows no peak shifts or splits, ruling out any intercalation processes in the early stages of discharge. Instead, all the reflections due to $Ni(PO_3)_2$ steadily decrease in intensity with increasing lithiation until they completely vanish at the end of the first discharge, demonstrating that the positive electrode eventually becomes

amorphous. Such amorphisation is commonly observed in conversion electrodes where the electrodes get electrochemically activated [5, 32]. No diffraction peaks of the conversion product $LiPO_3$ are observed by XRD, confirming its amorphous/glassy nature in agreement with our TEM observations. As for the in-house XRD pattern of the lithiated $Ni(PO_3)_2$ electrode (Figure S1), Ni metal formed during the conversion reaction is also undetectable by synchrotron XRPD, despite the much higher X-ray intensity, because the Ni nanodomains are too small [9, 33-34].

The electrochemical performance of the $Ni(PO_3)_2$ positive electrode were then evaluated over the voltage range 1.0-3.7 V. As shown in Figure 5a, a high capacity of 250 mAh/g is obtained in the 2nd cycle when the cell is tested at 0.1 C. This compares very well to the theoretical capacity of 247 mAh/g. The voltage profiles for the 2nd cycle show an average discharge voltage of ~2 V and average charge voltage of ~2.8 V. The large voltage gap (0.8 V) is typical for conversion systems, and is caused by different spatial evolution of the electrochemically active phases controlled by different reaction kinetics between conversion and de-conversion processes, according to previous research [3]. A capacity of 480 mAh/g, much higher than the theoretical value, is achieved in the first discharge. This is common in conversion systems due to electrolyte decomposition [5, 35]. Although the carbonate-based electrolyte is usually stable at above 1 V, metallic Ni formed in the conversion reaction probably catalyses its decomposition at these higher voltages. Strategies such as carbon coating [36-37] have been demonstrated to effectively supress, even eliminate electrode-induced electrolyte decomposition, which should be explored in the future development of $Ni(PO_3)_2$ as a positive electrode.

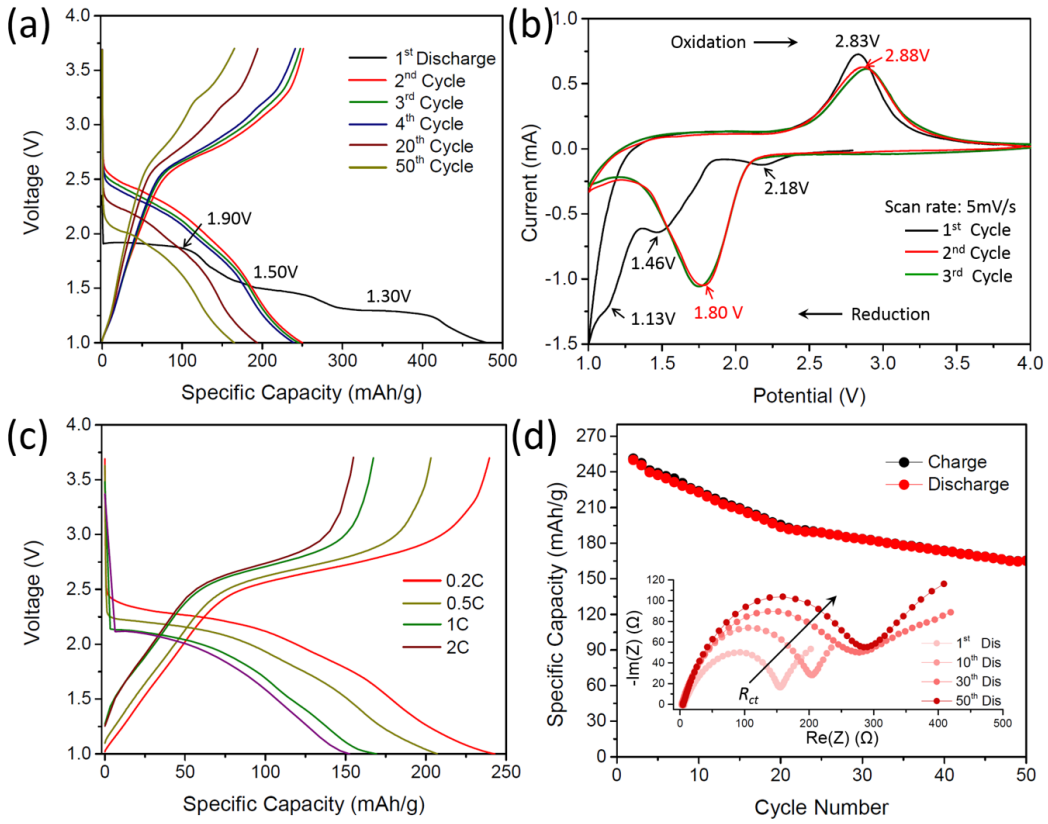

Figure 5 The electrochemical performance of the $Ni(PO_3)_2$ positive electrode: (a) voltage profiles of the selected cycles at 0.1C; (b) cyclic voltammetry curves for the first three cycles at a scan rate of 5 mV/s; (c) voltage profiles of the second cycles at various current rates; (d) cycling performance over 50 cycles at 0.1 C and Nyquist plots of the electrochemical impedance spectra collected from the $Ni(PO_3)_2$/Li cell at ends of discharging in selected cycles (insert).

The form of the voltage profile in the first discharge is also quite distinct from subsequent discharges, with three voltage plateaus at 1.9 V, 1.5 V, and 1.3 V. Similarly, Figure 5b shows three reduction peaks at 2.18 V, 1.46 V, and 1.13 V on the first discharge curve which are not seen in subsequent curves. These differences are unsurprising given that lithiation in the first discharge is accompanied by an irreversible amorphisation process. In an intercalation electrode,

three reduction peaks (or three plateaus in the voltage profile) would point to three distinct two-phase reactions – *i.e.*, the formation of two intermediate phases with stoichiometric partial Li occupancy, such as $Li_2Ti_4^{3+/4+}O_8$ ($Li_{0.5}TiO_2$) formed during the lithiation of anatase $Ti^{4+}O_2$ to $Li_4Ti_4^{3+}O_8$ ($LiTiO_2$)[38-39]. However, in this case, our XAS data have already ruled out an intermediate oxidation state of Ni between 2+ and 0; and our XRD data have ruled out any intermediate $Li_{2x}^{1+}Ni_{1-x}^{2+}(PO_3)_2$ phases. We therefore tentatively ascribe the three stages in the first lithiation of $Ni(PO_3)_2$ to three successively more efficient charge transport processes, which serve to reduce activation barriers and hence the voltage of the conversion reaction. A plausible scenario is that in the first stage, charge transfer is primarily due to slow Li^+ ion diffusion through crystalline $Ni(PO_3)_2$ grains; in the second stage, sufficient glassy $LiPO_3$ has formed that its excellent Li^+ conduction becomes the dominant charge transfer process; and in the third stage, reduced Ni metal at the grain boundaries reaches the percolation threshold for electronic conduction. Direct evidence for (or against) this scenario will require an *in situ* electrochemical TEM study, but this lies beyond the scope of the present work and does not directly impact its key results. The amorphisation process is complete after the first lithiation, crystalline $Ni(PO_3)_2$ does not re-form in any observable quantity, and subsequent dis/charge cycles take place in a homogenised matrix, explaining the observation of only one reduction peak at ~1.8 V.

Figure 5c shows the second-cycle voltage profiles of $Ni(PO_3)_2$ positive electrodes at various current rates. As can be seen, high capacities of 243 mAh/g and 207 mAh/g are obtained at 0.2 C and 0.5 C, respectively. Even at a high rate of 2 C, a high capacity of 152 mAh/g is achieved. According to previous reports, monoanion-type conversion electrodes often show a substantial capacity degradation at high currents due to kinetic limitations of diffusion driven processes during de-/lithiation[4-5, 34], but this is not the case for the polyanion-type $Ni(PO_3)_2$ positive

electrode. The superior ability to achieve high capacities at high rates can at least partly be ascribed to the low iconicity of the bond between $[PO_3]^-$ and Ni^{2+}, allowing fast diffusion kinetics during the conversion reaction with Li^+ ions. Furthermore, the $LiPO_3$ glass formed during the conversion reaction is a good Li^+ conductor, which facilitates the de-conversion process. Figure S2 shows the rate performance of the $Ni(PO_3)_2$ positive electrode. Although the electrode suffers a capacity reduction caused from both cycling and the programed increase of the current rate, a high capacity of 135 mAh/g is obtained when the rate is altered to 2C.

The cycling performance of the $Ni(PO_3)_2$ positive electrode shown in Figure 5d demonstrates a continuous fading over 50 cycles, implying a progressive degradation of the $Ni(PO_3)_2$ electrode. Specifically, the discharge capacity decreases to 158 mAh/g in the 50^{th} cycle, which corresponds to a capacity retention of 63.2%. The Nyquist plots of EIS data in the insert in Figure 5d shows a rising trend of the charge transfer impedance (R_{ct}) of the discharged $Ni(PO_3)_2$/Li cell over cycling, which is generally related to a gradual breakdown of the electron conduction network within the electrode.

To investigate the degradation of the $Ni(PO_3)_2$ positive electrode over cycling, *ex situ* XANES measurements were conducted on delithiated electrodes after varying numbers of discharges. As shown in Figure 6a, the intensity of the main absorption peak in the Ni K-edge XANES spectrum decreases with the increase of cycle numbers. Correspondingly, the Ni^{2+} content of the delithated electrode, which is estimated by fitting the spectrum using the LCF method, declines over cycling (see Figure 6b). The results reveal that the Ni metal formed in the previous conversion process does not completely convert back to Ni^{2+} in the following de-conversion process. We fit the trends of both the Ni^{2+} content and the capacity retention rate against the cycle number by the Equation S1 and plotted the results (Table S3) in Figure 6b. Two fitting plots closely following

each other in the whole range indicates that the accumulation of inactive Ni metal over cycling is the main cause of reduced electrochemical activation of the $Ni(PO_3)_2$ positive electrode and therefore of capacity fading. Over the extended range of 100-150 cycles, both plots approach saturation, suggesting that the $Ni(PO_3)_2$ electrode tends to an equilibrium state with approximately 0.6 of the active Ni^{2+}/Ni content eventually archiving a reversible capacity of approximately 60% of the original value. This projected value is confirmed by the capacity retention of a $Ni(PO_3)_2$ electrode over 100 cycles (60.3%) (see Figure S3). The equilibrium is likely driven by a complex interplay between the surface energy of Ni domains, the activation energy of diffusion, and the elemental distribution in the composite formed.

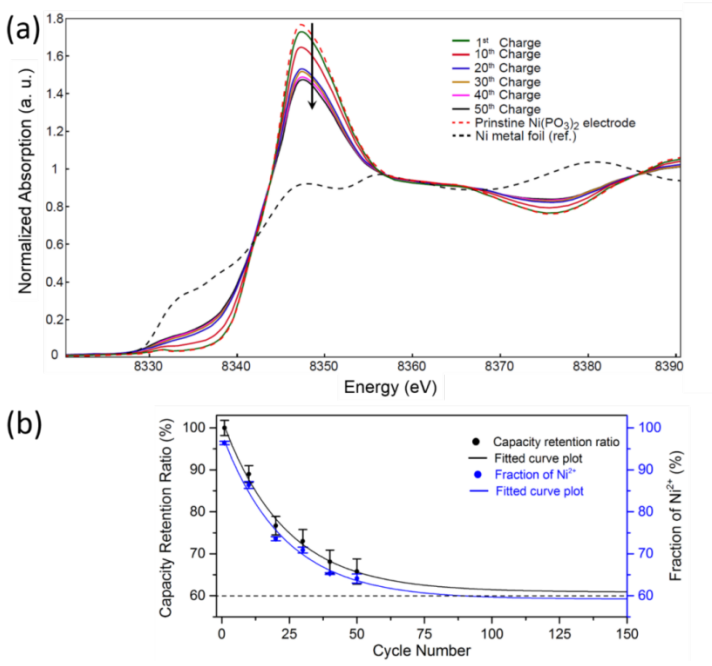

Figure 6 (a) Ni K-edge XANES spectra collected from the de-lithiated $Ni(PO_3)_2$ electrodes with selected cycle numbers (1, and every tenth from 10 to 50). Spectra were collected from electrodes of the same mass to ensure a valid comparison. (b) Fitted plots of both the fraction of Ni^{2+} in the de-lithiated $Ni(PO_3)_2$ electrode and the capacity retention against cycle number.

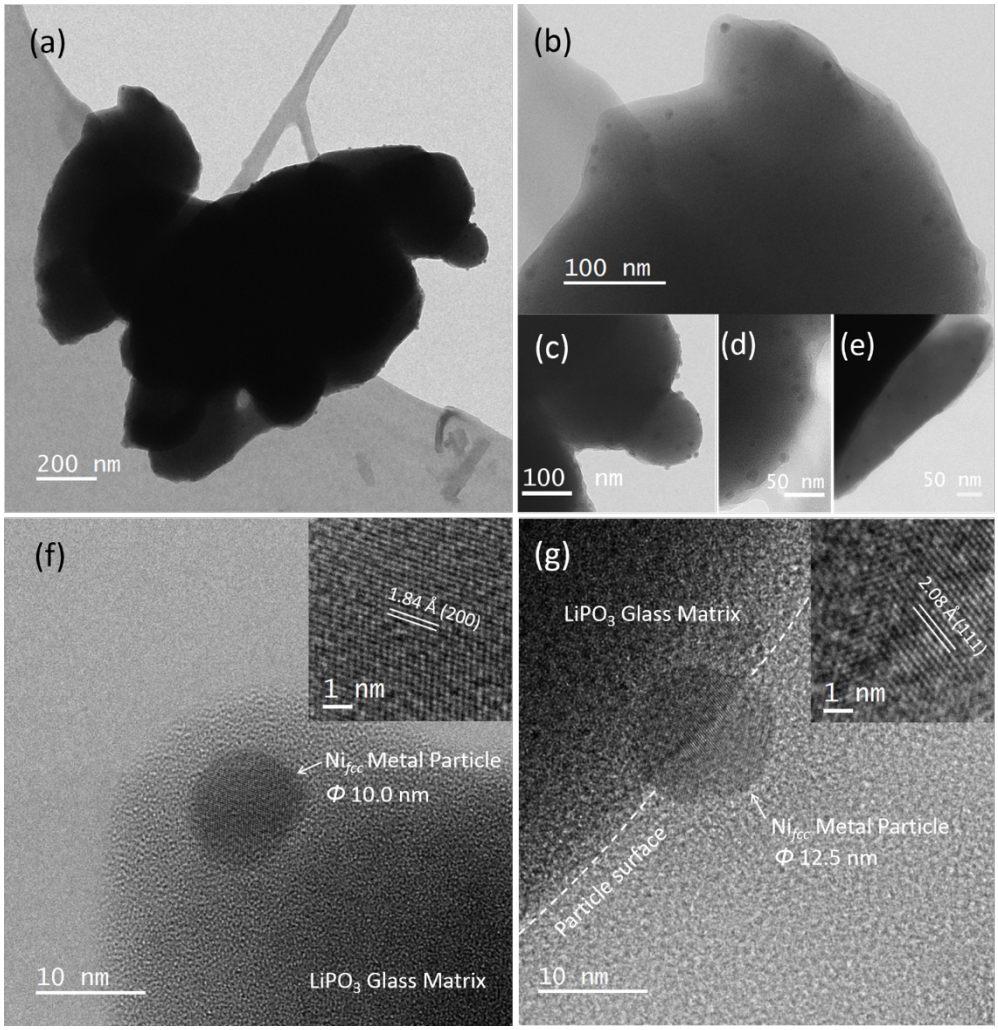

Figure 7 HRTEM images of the lithiated $Ni(PO_3)_2$ electrode after the 50th discharge: (a) a low-magnification image of a particle aggregate; (b)-(e) high-magnification images of the selected regions on particles depicted in (a); and high-magnification images and lattice fringe images (inserts) of (f) a metallic Ni particle located in the bulk of $LiPO_3$ glass matrix and (g) one which is half-exposed on the surface.

HRTEM was used to study the morphology and distribution of Ni metal in the lithiated $Ni(PO_3)_2$ electrode after the 50th discharge. As shown in Figures 7a-e, in this electrode, Ni nanograins with

a spherical shape and a size of ~10 nm are randomly dispersed in the $LiPO_3$ glass matrix, well-separated from each other. Compared to Ni nanodomains formed in the first lithiation, these Ni metal nanograins are much larger in size, more regular in shape, and have higher crystallinity. The magnified image in Figure 7f shows a single large spherical nanograin with no smaller grains in the vicinity. This microstructure no longer supports a percolating Ni metal network, resulting in increased electron transport resistance, explaining our EIS results (R_{ct} increases with cycling). As can be seen clearly in Figure 7a, 7c, 7d and 7g, some Ni grains are partially exposed on the surface of the electrode particles, further isolating them from the $LiPO_3$ glass matrix and therefore increasing the mass transfer resistance barrier to the formation of $Ni(PO_3)_2$, so that complete de-conversion is not readily achieved. Figures 7g-f also show that the large Ni nanograins after the 50^{th} lithiation are much more crystalline than the nanodomains after the first lithiation. The formation of such well-crystallised large spherical grains under relatively mild electrochemical conditions strongly suggests nucleation on unreacted Ni metal from previous cycles.

Conclusions

We have shown that nickel (II) metaphosphate $Ni(PO_3)_2$ is an effective conversion positive electrode for use in lithium-ion batteries. To the best of our knowledge, this is the first polyanion-type conversion positive electrode to be discovered. Compared to monoanion-type fluoride conversion positive electrodes, $Ni(PO_3)_2$ exhibits much better intrinsic electrochemical activity, due to a combination of the low ionicity of the Ni-[PO_3] bond allowing faster reaction kinetics and the fact that glassy $LiPO_3$, formed during the conversion reaction, is itself an excellent Li^+ conductor. A close-to-theoretical capacity of 250 mAh/g and an average discharge

voltage of 2 V were achieved at a current rate of 0.1 C at room temperature using micro-sized $Ni(PO_3)_2$ powders synthesised by a low-cost solid-state method. A good rate performance was also achieved. We systematically studied the conversion reaction of $Ni(PO_3)_2$ with Li^+ using a combination of XPS, FTIR, *in situ* XANES, *in situ* XRPD and *ex situ* HRTEM characterisation. During the first discharge, crystalline $Ni(PO_3)_2$ is electrochemically activated through a Li^+-driven amorphization process along with the reduction of Ni^{2+} to metallic Ni. P does not participate electrochemically, remaining as P^{5+} in $[PO_3]^-$ throughout. A fine microstructure consisting of polygon-shaped Ni nanodomains with a width of ~2 nm embedded into a $LiPO_3$ glass matrix was formed in the lithiated electrode. During the following first charge, the electrode converts compositionally back to $Ni(PO_3)_2$ but does not recrystallise. The positive electrode eventually remains amorphous, in which state it can reversibly store lithium.

Like other conversion electrodes, $Ni(PO_3)_2$ undergoes a noticeable capacity fade caused by electrode degradation. A combined EIS, *ex situ* XANES, and HRTEM study revealed that the fraction of residual Ni metal in the delithiated electrodes increases over cycling. Newly formed Ni metal nucleates on residual Ni metal grains from previous conversion processes, which grow larger and more crystalline with each cycle. However, this process tends to saturation at a projected capacity of ~150 mAh/g, *i.e.*, ~60 % of the original value. In future work, we will focus on materials optimisation to design and synthesise higher-entropy Ni-based solid-solution metaphosphates that suppress this grain growth and improve the cycling stability. Another approach that has shown promise in similar cases of materials with high electrochemical activity or Li^+ conductivity but low theoretical capacity is to combine them with materials that have high theoretical capacities but low electrochemical activity, to make composite conversion electrodes with much better comprehensive performance than their components [40-41]. In this case, metal

fluorides such as NiF_2, FeF_2 and FeF_3 are plausible choices that we will explore using strategies such as high-energy ball-milling.

Acknowledgements

This work was supported by the Australian Research Council – Discovery Projects (DP200100959). Q. X. thanks ANSTO and Sydney Nano Institute for scholarship support. Part of this research was performed on the PD and XAS Beamlines at the Australian Synchrotron, part of the Australian Nuclear Science and Technology Organisation (ANSTO). This research was facilitated by access to Sydney Analytical, a core research facility at the University of Sydney.

References

[1] G. E. Blomgren, *J. Electrochem. Soc.* **2017**, *164*, A5019-A5025.
[2] M. Li, J. Lu, Z. W. Chen, K. Amine, *Adv. Mater.* **2018**, *30,* 1800561.
[3] L. S. Li, R. Jacobs, P. Gao, L. Y. Gan, F. Wang, D. Morgan, S. Jin, *J. Am. Chem. Soc.* **2016**, *138*, 2838-2848.
[4] J. Cabana, L. Monconduit, D. Larcher, M. R. Palacin, *Adv. Mater.* **2010**, *22*, E170-E192.
[5] A. Kraytsberg, Y. Ein-Eli, *J. Solid State Electr.* **2017**, *21*, 1907-1923.
[6] R. Hausbrand, G. Cherkashinin, H. Ehrenberg, M. Groting, K. Albe, C. Hess, W. Jaegermann, *Mater. Sci. Eng. B-Adv.* **2015**, *192*, 3-25.
[7] A. M. Haregewoin, A. S. Wotango, B. J. Hwang, *Energ. Environ. Sci.* **2016**, *9*, 1955-1988.
[8] F. Badway, F. Cosandey, N. Pereira, G. G. Amatucci, *J. Electrochem. Soc.* **2003**, *150*, A1318-A1327.
[9] F. Wang, R. Robert, N. A. Chernova, N. Pereira, F. Omenya, F. Badway, X. Hua, M. Ruotolo, R. G. Zhang, L. J. Wu, V. Volkov, D. Su, B. Key, M. S. Whittingharn, C. P. Grey, G. G. Amatucci, Y. M. Zhu, J. Graetz, *J. Am. Chem. Soc.* **2011**, *133*, 18828-18836.
[10] L. S. Li, F. Meng, S. Jin, *Nano Lett.* **2012**, *12*, 6030-6037.
[11] S. W. Kim, D. H. Seo, H. Gwon, J. Kim, K. Kang, *Adv. Mater.* **2010**, *22*, 5260-5264.
[12] A. Rosenman, E. Markevich, G. Salitra, D. Aurbach, A. Garsuch, F. F. Chesneau, *Adv. Energy Mater.* **2015**, *5,* 500212.
[13] M. Wild, L. O'Neill, T. Zhang, R. Purkayastha, G. Minton, M. Marinescu, G. J. Offer, *Energ. Environ. Sci.* **2015**, *8*, 3477-3494.

[14] C. Villa, S. K. Kim, Y. X. Lu, V. P. Dravid, J. S. Wu, *Acs. Appl. Mater. Inter.* **2019**, *11*, 647-654.
[15] Y. V. Mikhaylik, J. R. Akridge, *J. Electrochem. Soc.* **2004**, *151*, A1969-A1976.
[16] W. B. Fu, E. B. Zhao, Z. F. Sun, X. L. Ren, A. Magasinski, G. Yushin, *Adv. Funct. Mater.* **2018**, *28*, 1801711.
[17] S. Peckham, N. Awofeso, *Sci. World J.* **2014**, *2014*, 293019.
[18] H. Arai, S. Okada, Y. Sakurai, J. Yamaki, *J. Power Sources* **1997**, *68*, 716-719.
[19] X. Zhao, C. M. Hayner, M. C. Kung, H. H. Kung, *Chem. Commun.* **2012**, *48*, 9909-9911.
[20] J. Liu, Y. L. Wan, W. Liu, Z. S. Ma, S. M. Ji, J. B. Wang, Y. C. Zhou, P. Hodgson, Y. C. Li, *J. Mater. Chem. A* **2013**, *1*, 1969-1975.
[21] X. Xu, W. Liu, Y. Kim, J. Cho, *Nano Today* **2014**, *9*, 604-630.
[22] A. Manthiram, Y. Fu, Y.-S. Su, *Acc. Chem. Res.* **2013**, *46*, 1125-1134.
[23] G. Xu, B. Ding, J. Pan, P. Nie, L. Shen, X. Zhang, *J. Mater. Chem. A* **2014**, *2*, 12662-12676.
[24] J. Ni, Y. Kawabe, M. Morishita, M. Watada, T. Sakai, *J. Power Sources* **2011**, *196*, 8104-8109.
[25] C. Hu, H. Yi, H. Fang, B. Yang, Y. Yao, W. Ma, Y. Dai, *Electrochem. Commun.* **2010**, *12*, 1784-1787.
[26] M. C. Simoes, K. J. Hughes, D. B. Ingham, L. Ma, M. Pourkashanian, *Inorg. Chem.* **2017**, *56*, 7566-7573.
[27] A. Olbertz, D. Stachel, I. Svoboda, H. Fuess, *Z. Krist-New Cryst. St.* **1998**, *213*, 241-242.
[28] W. S. Yoon, M. Balasubramanian, K. Y. Chung, X. Q. Yang, J. McBreen, C. P. Grey, D. A. Fischer, *J. Am. Chem. Soc.* **2005**, *127*, 17479-17487.
[29] B. K. Money, K. Hariharan, *Integr. Ferroelectr.* **2010**, *120*, 75-89.
[30] E. Kartini, T. Y. S. P. Putra, I. Kuntoro, T. Sakuma, K. Basar, O. Kamishima, J. Kawamura, *J. Phys. Soc. Jpn* **2010**, *79*, 54-58.
[31] E. Kartini, M. Nakamura, M. Arai, Y. Inamura, K. Nakajima, T. Maksum, W. Honggowiranto, T. Y. S. P. Putra, *Solid State Ion.* **2014**, *262*, 833-836.
[32] M. V. Reddy, G. V. S. Rao, B. V. R. Chowdari, *Chem. Rev.* **2013**, *113*, 5364-5457.
[33] P. Poizot, S. Laruelle, S. Grugeon, L. Dupont, J. M. Tarascon, *Nature* **2000**, *407*, 496-499.
[34] A. Sarkar, L. Velasco, D. Wang, Q. S. Wang, G. Talasila, L. de Biasi, C. Kubel, T. Brezesinski, S. S. Bhattacharya, H. Hahn, B. Breitung, *Nat. Commun.* **2018**, *9*, 3400.
[35] S. Laruelle, S. Grugeon, P. Poizot, M. Dolle, L. Dupont, J. M. Tarascon, *J. Electrochem. Soc.* **2002**, *149*, A627-A634.
[36] Y. B. He, F. Ning, B. H. Li, Q. S. Song, W. Lv, H. D. Du, D. Y. Zhai, F. Y. Su, Q. H. Yang, F. Y. Kang, *J. Power Sources* **2012**, *202*, 253-261.
[37] H. Q. Li, H. S. Zhou, *Chem. Commun.* **2012**, *48*, 1201-1217.
[38] R. van de Krol, A. Goossens, J. Schoonman, *J. Phys. Chem. B* **1999**, *103*, 7151-7159.
[39] M. H. Zhang, K. B. Yin, Z. D. Hood, Z. H. Bi, C. A. Bridges, S. Dai, Y. S. Meng, M. P. Paranthaman, M. F. Chi, *J. Mater. Chem. A* **2017**, *5*, 20651-20657.
[40] A. El Kharbachi, H. Uesato, H. Kawai, S. Wenner, H. Miyaoka, M. H. Sorby, H. Fjellvag, T. Ichikawa, B. C. Hauback, *Rsc. Adv.* **2018**, *8*, 23468-23474.
[41] W. R. Liu, N. L. Wu, D. T. Shieh, H. C. Wu, M. H. Yang, C. Korepp, J. O. Besenhard, M. Winter, *J. Electrochem. Soc.* **2007**, *154*, A97-A102.